A00-16418

AIAA 2000-0539
Direct Numerical Simulation of Instability of Nonequilibrium Reacting Hypersonic Boundary Layers

Yanbao Ma and Xiaolin Zhong
University of California, Los Angeles

38th Aerospace Sciences Meeting & Exhibit
January 10–13, 2000 / Reno, NV

Direct Numerical Simulation of Instability of Nonequilibrium Reacting Hypersonic Boundary Layers

Yanbao Ma*and Xiaolin Zhong†

University of California, Los Angeles, CA 90095

Abstract

In high Mach number flight conditions, air begins to depart from the perfect gas behavior due to vibrational excitation and chemical dissociation, which can significantly influence the heat flux on the vehicle wall surface and laminar-turbulent transition. In our previous work, fifth-order upwind finite difference scheme combined with additive semi-implicit Runge-Kutta method is developed and validated in direct simulation of transient hypersonic nonequilibrium flows. This method is advanced and applied for the nonequilibrium hypersonic flow over a thin flat plate. Unsteady flow is developed naturely after disturbance is introduced by blowing and suction through a narrow slot on the wall. The numerical methods and computational codes are validated by comparing the results with locally self-similar boundary layer results and local linear stability analysis.

Introduction

The laminar-turbulent transition in hypersonic boundary layer significantly affects the dynamic performance and surface heating of space transportation vehicles. Therefore, the accurate prediction of boundary layer transition is a critical part of the aerodynamic design of advanced hypersonic vehicles and corresponding thermal protection system. The transition from laminar to turbulent flow in wall-bounded shear layers occurs because of an incipient instability of the basic flow field, which is identified in stability analyses. In general, the transition is a result of nonlinear response of the laminar boundary layers to forcing disturbances [1–4]. The forcing disturbances can originate from many different sources, including disturbance in free stream, and blowing and suction through the slot on the wall. Initially these disturbances may be too small to be measured, and they can be observed only after the onset of an instability. The initial growth of these disturbances is described by linear stability theory (LST). The properties of disturbance can be described by defining a local Mach number $\bar{M}$ according to the disturbance phase speed c_r relative to the boundary layer edge velocity u_e:

$$\bar{M} = \frac{u_e - c_r}{a_e} \tag{1}$$

where a_e is the sound speed at the edge of the boundary layer. When the local flow velocity is subsonic throughout the boundary layer relative to the disturbance phase speed ($\bar{M} < 1$), the presence of a generalized inflection point (gip), defined as:

$$\frac{\partial}{\partial y}\left(\rho \frac{\partial u}{\partial y}\right) = 0 \tag{2}$$

is a sufficient condition for the existence of instability (first mode) because of a maximum in the angular momentum according to Lee and Lin's [5] results. The first mode is an extension of the incompressible Tollmien-Schlichting (TS) wave at high speeds. After the pioneering work of Lee and Lin, Mack [6,7] made great contributions to the subject on compressible boundary layer stability. Mack developed the theory for compressible flat plate flow and obtained fruitful results about the effects of Mach number, wall temperature, Reynolds number *etc.* For compressible gas flows, the inflection point moves away from the wall boundary with the increasing Mach number. As a result, the first mode inviscid instability increases. This effect occurs up to a Mach number of approximately 5 [7]. At supersonic Mach number, the fist mode represents a combination of the viscous (TS) mode and the inviscid compressible Rayleigh instability associated with the general inflection point in the basic flow profiles. At high Mach number, besides of first mode, Mack found a new family of unstable modes called Mach modes, which represent sound waves that reflect inviscidly between the solid wall and the relative sonic

*Graduate Student Researcher, Department of Mechanical and Aerospace Engineering

†Associate Professor, Department of Mechanical and Aerospace Engineering, Senior Member AIAA.

line in the boundary layer [8]. The second inviscid stability mode is caused by the presence of a region of supersonic mean flow relative to the disturbance phase velocity. At higher Mach number, higher modes belonging to this class may be relevant. Mack investigated the effects of wall temperature and found that the wall cooling is stablizing to the first mode while destabilizing to the second mode. Some later work on compressible stability of axisymmetric boundary layers can be found in Refs. [8–13]. The recent advancement on stability of boundary layer is reviewed in Ref. [14].

The stability of hypersonic flow is much more complicated due to vibrational excitation and chemical reaction. In hypersonic flows, the bow shock is pushed more closely to the edge of the boundary layer. The real gas effects on stability were investigated by Malik [15,16] by assuming air to be in thermal and chemical equilibrium. Stuckert and Reed [17] studied the effects of finite rate chemistry on stability of shock layer with basic state being taken to be the solution of the parabolized Navier-Stokes(PNS) equations. They also considered the effect of shock by using the linearized shock-jump conditions. Recently, Hudson et al. [18] analyzed the stability of hypersonic flat plate boundary layer by assuming both chemical and thermal nonequilibrium. All these numerical results showed that the effect of chemical reaction is very similar to that of wall cooling, *i.e.*, stablizing for the first mode and destabilizing for the second mode. In addition, the second mode is shifted to lower frequencies shown in both the equilibrium and nonequilibrium air calculations. This is attributed to the increase in the size of the region of relative supersonic flow due to the lower speeds of sound in the relatively cooler boundary layers.

Many theoretical and experimental studies have been done on hypersonic boundary layer transition. Reshotko and Khan [19] showed that the swallowing of the entropy layer by the boundary layer has strong effects on the stability of the boundary layers. The experimental measurement on hypersonic boundary layer stability of sharp cones showed the additional complexity of hypersonic boundary layers [20–22]. The results indicated that the first and second mode instabilities are simultaneously present in the hypersonic boundary layers. Experiments on hypersonic boundary layer transition of blunt cones [23–25] showed that slight nose bluntness has significant effects on the boundary layer transition. The increase of nose bluntness delays the transition onset, but the trend is reversed when the nose bluntness exceeds a certain limit. In addition, Stetson et al. [25] found the evidence of inviscid entropy instability in the region outside of the boundary layers for the case of certain blunt cones at Mach 8 free stream in the entropy-layer swallowing region. The stability characteristics of hypersonic boundary layers over a blunt cone corresponding to Stetson's experiments [25] have been studied using LST by Malik et al. [10], Herbert and Esfahanian [26], and Kufner et al. [27,28]. Though some observations on the effects of bluntness and the entropy layer are consistent with linear stability analysis, the second-mode instability and the general amplification characteristics in the blunt cone flows do not agree with the experiments. The discrepancy may be due to the fact that the LST of hypersonic flow over a blunt cone has the difficulty of obtaining highly-accurate steady base flow for the stability equations.

Although the parabolized stability equations(PSE) results of Bertolotti [29] and Chang et al. [30], which accounts for the nonparallel and nonlinear effects, showed that nonparallel effects are negligible for 2-D waves on a flat plate compared with the stability results of El-hady [31] and Arnal [32], nonparallelism has strong destabilizing effect for oblique waves. This effect increases with increasing Mach number [29,33,34]. More recently, Chang et al. [35] investigated the effect of reacting chemistry on the instability waves and supersonic mode instability that is characterized by an oscillating disturbance structure outside of the boundary layer and a relative phase velocity faster than the free-stream sonic speed. PSE has shown promise to calculate boundary layer transition. However, both linear and parabolized stability stability analyses are very sensitive to the accuracy of the base flows. In addition, the effects of the bow shock , nonlinear interaction and non-parallel boundary layers on the disturbances fields are not completely considered in the LST and PSE. LST and PSE could not deal with the process that acoustic, vorticity or entropy disturbances in free stream enter the boundary layer as fluctuation of the basic state, which is called receptivity [36,37]. This part of the process provides the vital initial conditions of amplitude, frequency, and phase for breakdown of laminar flow. Transition to turbulence will never be successfully understood or predicted without answering how free-stream disturbances enter the boundary layer and ultimately generate unstable waves.

For hypersonic flow over blunt bodies, the receptivity phenomena are much more complex and are currently still poorly understood [38,39]. Kovasznay [40] showed that weak disturbance waves in compressible flow can be decomposed into three independent modes: acoustic, entropy, and vorticity modes. The acoustic waves propagate with the speed of sound relative to the moving fluid, while the entropy and vorticity waves convect with the moving fluid velocity. Before entering the boundary layer, free stream disturbances will be first processed by the bow shock. Irrespective of the

nature of the free stream disturbance, its interaction with the bow shock always generates all three types of waves [41]. These transmitted disturbance waves propagate to downstream and interact with the boundary layer near the body. At the same time, the boundary layer will also generate reflected acoustic wave impinging on the shock from behind and generating further disturbances to the shock and wave fields. All these interactions will affect the transition of the hypersonic boundary layer behind the shock. The review of recent progress in this area can be found in Ref. [42–45]. Receptivity of nonequilibrium hypersonic flow remains unresolved and deserves more systematic investigation in light of its importance to the prediction of transition.

At the first step, we investigate the the hypersonic flow over a thin flat plate. In the downstream, the shock layer and boundary layer are separated from each other and clearly distinguishable. To simplify the problem, shock layer is excluded from the computational domain. The objective of this research is to investigate the stability of nonequilibrium hypersonic flow by direct numerical simulation using high-order upwind finite difference methods. Semi-implicit method is used to treat source terms due to chemical reaction and excitation of vibrational energy. The numerical methods and computational code were validated in calculation of hypersonic flow over a blunt body [46].

Our main purpose is to study the real gas effects on the stability of hypersonic flow. The departure from perfect gas depends on temperature as well as pressure. For example, at a pressure of 1 atm, vibrational excitation begins at about $800°K$. When temperature exceeds about $2500°K$, oxygen moleculae begin to dissociate while nitrogen begins at about $4000°K$. Reacting oxygen flow instead of air flow over a flat plate is studied in this work for the purpose of computational expediency. In order to validate our code for simulation of flow over a flat plate, we also study the hypersonic reacting flow via boundary layer approach under local self-similarity assumption. The pressure gradients induced by interaction of external free stream and viscous boundary layer flow is modeled by prediction-correction scheme.

After obtaining the mean flow, we introduce the disturbance by blowing and suction through a narrow slot on the wall. In order to analysis the real gas effects, we also study the same problem under the perfect gas regime.

Governing Equations and Physical Model

The governing equations are formulated for a two-temperature model with two species (non-ionizing) finite rate chemistry under the assumption that the rate of rotational relaxation approachs infinity, and the rotational energy is fully excited (*i.e.*, rotational temperature equals translational temperature).

Direct Numerical Simulation

In conservative form, the two-dimensional Navier-Stokes equation can be written as:

$$\frac{\partial \mathbf{U}}{\partial t} + \frac{\partial}{\partial x}(\mathbf{F_1} + \mathbf{F_{v1}}) + \frac{\partial}{\partial y}(\mathbf{F_2} + \mathbf{F_{v2}}) = \mathbf{W} \quad (3)$$

where the conserved quantity and source term vectors are:

$$\mathbf{U} = \begin{bmatrix} \rho_1 \\ \rho_2 \\ \rho u \\ \rho v \\ E_v \\ E \end{bmatrix}, \qquad \mathbf{W} = \begin{bmatrix} w_1 \\ -w_1 \\ 0 \\ 0 \\ w_v \\ 0 \end{bmatrix}. \quad (4)$$

Inviscid fluxes are

$$\mathbf{F_1} = \begin{bmatrix} \rho_1 u \\ \rho_2 \\ \rho u^2 + p \\ \rho uv \\ uE_v \\ u(E+p) \end{bmatrix}, \quad \mathbf{F_2} = \begin{bmatrix} \rho_1 v \\ \rho_2 v \\ \rho uv \\ \rho v^2 + p \\ vE_v \\ v(E+p) \end{bmatrix}. \quad (5)$$

Viscous and diffusive fluxes are

$$\mathbf{F_{v1}} = \begin{bmatrix} j_{1x} \\ j_{2x} \\ -\tau_{xx} \\ -\tau_{xy} \\ q_{vx} \\ Q_x \end{bmatrix}, \quad \mathbf{F_{v2}} = \begin{bmatrix} j_{1y} \\ j_{2y} \\ -\tau_{xy} \\ -\tau_{yy} \\ q_{vy} \\ Q_y \end{bmatrix}. \quad (6)$$

where

$$\begin{aligned} Q_x &= -u\tau_{xx} - v\tau_{xy} + q_x, \\ Q_y &= -u\tau_{xy} - v\tau_{yy} + q_y. \end{aligned} \quad (7)$$

Boundary Layer Approach

Under the boundary layer assumption, the governing equations can be simplified as the following:

$$\frac{\partial}{\partial x}(\rho u) + \frac{\partial}{\partial y}(\rho v) = 0 \quad (8)$$

$$\frac{\partial}{\partial x}(\rho_1 u) + \frac{\partial}{\partial y}(\rho_1 v + j_{1y}) = w_1 \quad (9)$$

$$\frac{\partial}{\partial x}(\rho u^2 + p) + \frac{\partial}{\partial y}(\rho uv - \mu\frac{\partial u}{\partial y}) = 0 \quad (10)$$

$$\frac{\partial}{\partial x}(uE_v) + \frac{\partial}{\partial y}(vE_v + q_{vy}) = w_v \quad (11)$$

$$\frac{\partial}{\partial x}[u(E+p)] + \frac{\partial}{\partial y}[v(E+p) - u\mu\frac{\partial u}{\partial y} + q_y] = 0 \quad (12)$$

State Equations and Source Terms

The system is taken to be a mixture of thermally perfect gases with the following equation of state:

$$p = \rho R T_t, \qquad \rho = \rho_1 + \rho_2 \quad (13)$$

where p and ρ are the bulk pressure and density, respectively, T_t is the translational temperature, and R is the mass averaged gas constant, defined as:

$$R = C_1 R_1 + C_2 R_2 \quad (14)$$

where $R_i (i = 1, 2)$ is the species specific gas constant, C_i the mass fraction. The vibrational and total energies per unit volume are given by:

$$E_v = \sum_{i=1}^{nd} \rho_i e_{vi}, \qquad E = \sum_{i=1}^{NS} \rho_i e_i + \rho\frac{u^2 + v^2}{2} \quad (15)$$

The reaction model is given as:

$$O_2 + M_i \quad \rightleftharpoons \quad O + O + M_i \quad (16)$$

where M_i denotes any of the i species. Reaction rates are following Park' chemistry model [47,48]. The components of total energy and transport coefficients are described in detail in our previous work [46].

Numerical Methods and Boundary Conditions

Direct Numerical Simulation

Fifth-order upwind finite difference schemes are applied for convective terms while sixth-order central schemes for the discretization of viscous terms [49].

The spatial discretization of the governing equations leads to a system of first-order ordinary differential equations. Third-order Semi-implicit Runge-Kutta schemes [50] are used for temporal discretization. The governing equations are additively split into stiff and non-stiff terms in the form of

$$\frac{d\mathbf{U}}{dt} = \mathbf{F}(\mathbf{U}) + \mathbf{G}(\mathbf{U}) \quad (17)$$

where $\mathbf{U}$ is the vector of discretized flow field variables, $\mathbf{F}$ is non-stiff terms resulted from spatial discretization of the flux terms which can be computed explicitly, and $\mathbf{G}$ is stiff thermo-chemical source terms which need to be computed implicitly.

For numerical simulation with source term, it is necessary to exactly evaluate the Jacobian of source vector $\mathbf{C} = \partial\mathbf{W}/\partial\mathbf{U}$. $\mathbf{W}$ can be expressed as a function of the temperature

$$\mathbf{W}(\mathbf{U}) = \tilde{\mathbf{W}}(\mathbf{U}, T(\mathbf{U}), T_v(\mathbf{U})), \quad (18)$$

and Jacobian can be written as

$$\mathbf{C} = \frac{\partial\tilde{\mathbf{W}}}{\partial\mathbf{U}} + \frac{\partial\tilde{\mathbf{W}}}{\partial T}\frac{\partial T}{\partial\mathbf{U}} + \frac{\partial\tilde{\mathbf{W}}}{\partial T_v}\frac{\partial T_v}{\partial\mathbf{U}} \quad (19)$$

The derivation of each term in more detail can be found in Ref. [51]

Boundary Conditions

Self-similar results of boundary layer solutions are used as inflow conditions. Non-slip, non catalytic and adiabatic wall condition is used at the wall boundary. Extrapolation is used as outflow condition because flow is hypersonic except that there exists a considerably small subsonic region near the wall. No reflecting characteristic boundary conditions are applied at the upper boundary. Equation (3) in the computational domain

at the upper boundary can be rewritten as:

$$\frac{\partial \mathbf{U}}{\partial t} = -\left(\frac{\partial}{\partial x}(\mathbf{F_1}+\mathbf{F_{v1}}) + \frac{\partial}{\partial y}(\mathbf{F_2}+\mathbf{F_{v2}}) - \mathbf{W}\right) \quad (20)$$

where the right side of the equation is valuated by one-sided finite difference scheme. In above equations, the Jacobian matrix, $\mathbf{B} = (\partial \mathbf{F_2}/\partial \mathbf{U})$, has the six eigenvalues:

$$\lambda_1 = \lambda_2 = \lambda_3 = \lambda_4 = v, \quad (21)$$
$$\lambda_5 = v + c, \quad \lambda_6 = v - c.$$

where c is the frozen speed of sound. The corresponding left eigenvectors can be written as

$$\mathbf{L1}, \quad \mathbf{L2}, \quad \mathbf{L3}, \quad \mathbf{L4}, \quad \mathbf{L5}, \quad \mathbf{L6} \quad (22)$$

Among them, the only incoming wave is associated with λ_6 [52], while others are outgoing waves associated with $\lambda_i (i = 1, 2, 3, 4, 5)$. The compatibility relations for these characteristic fields can be obtained by multiplying Eq. (20) with $\mathbf{Li}(i = 1, 2, 3, 4, 5)$,

$$\mathbf{Li} \cdot \frac{\partial \mathbf{U}}{\partial t} = -\mathbf{Li} \cdot \left(\frac{\partial}{\partial x}(\mathbf{F_1}+\mathbf{F_{v1}}) + \frac{\partial}{\partial y}(\mathbf{F_2}+\mathbf{F_{v2}}) - \mathbf{W}\right) \quad (23)$$

which gives five equations for six unknows. Non-reflecting condition is enforced here to enclose equations,

$$\frac{\partial p}{\partial t} - \rho c \frac{\partial v}{\partial t} = 0. \quad (24)$$

The expression of Jacobian matrix $\mathbf{B}$ and left eigenvectors can be found in Ref. [53].

Boundary Layer Approach

We choose Illingworth transformation and the following dimensionless dependent variables in order to get locally self-similar solutions.

$$\xi = \int_0^x \rho_e u_e \mu_e dx \quad (25)$$

$$\eta = \frac{u_e \int_0^y \rho dy}{\sqrt{2\xi}} \quad (26)$$

$$f_\eta = \frac{u}{u_e} \quad (27)$$

$$g = \frac{T}{T_e} \quad (28)$$

$$g_v = \frac{T_v}{T_{ve}} \quad (29)$$

$$s_1 = \frac{C_1}{C_{1e}} \quad (30)$$

where the subscript e refers to the values in the local free stream, and C_1, C_2 are the mass fraction of molecular and atomic oxygen respectively. Substituting in boundary layer equations and assuming the dependent variables f, g, g_v, s_1 are functions of η alone, there results

$$[l f_{\eta\eta}]_\eta + f f_{\eta\eta} + \beta_1 g \frac{1+C_2}{1+C_{2e}} - \beta_1 f_\eta^2 = 0 \quad (31)$$

$$\left[\frac{l L_1 s_{1\eta}}{P_r}\right]_\eta + f s_{1\eta} + \zeta \frac{w_1}{\rho C_{1e}} = 0 \quad (32)$$

$$\left[\frac{l C_p g_\eta}{C_{pe} P_r}\right]_\eta + \frac{C_p}{C_{pe}} f g_\eta - \zeta \frac{\sum_{i=1}^{2}(h_i - e_{vi}) w_i + w_v}{\rho C_{pe} T_e} + \beta_2 f_{\eta\eta}^2 + \sum_{i=1}^{2} \frac{l C_{pi} L_i C_{i\eta} g_\eta}{C_{pe} P_r} = 0 \quad (33)$$

$$[l_1 g_{v\eta}]_\eta + \frac{C_{vv} C_1}{C_{pe}} f g_{v\eta} - \frac{l C_{vv} C_1 L_1}{C_{pe} P_r} s_{1\eta} g_{v\eta} + \zeta \frac{Q_{T-V}}{\rho C_{pe} T_e} = 0 \quad (34)$$

where

$$l = \frac{\rho \mu}{\rho_e \mu_e}, \quad (35)$$

$$\beta_1 = \frac{2\xi}{ue} \frac{\partial u_e}{\partial \xi}, \quad (36)$$

$$\zeta = \frac{2\xi}{u_e \xi_x}, \quad (37)$$

$$\beta_2 = \frac{l u_e^2}{C_{pe} T_e}, \quad (38)$$

$$C_p = C_1 C_{p1} + C_2 C_{p2}, \quad (39)$$

$$P_r = \frac{C_p \mu}{k}, \quad (40)$$

$$L_i = \frac{\rho D_i C_p}{k}, \quad (41)$$

$$l_1 = \frac{l k_{v1} C_p C_1 g_{v\eta}}{(k_t + k_r) P_r C_{pe}}, \quad (42)$$

$$C_{vv} = \frac{k_{v1}}{\mu_1}. \quad (43)$$

Eqs. (31) to (34) were solved simultaneously by using Chebyshev collocation spectral method with the boundary conditions

$f(0) = 0, f_\eta(0) = 0, f_\eta(\infty) = 1,$
$s_{1\eta}(0) = 0, s_{1\infty} = 1,$
$g(0) = g_v(0) = g_w$(isothermal wall) ,
$g_\eta = g_{v\eta} = 0$(adiabatic wall),
$g(\infty) = g_v(\infty) = 1.$

Then, the vertical velocity is calculated numerically through continuous equation.

In hypersonic viscous flow, the curvature of the boundary layer brings about an important change in the effective geometric shape of the body, which results that pressure variations are propagated into the main free stream along the Mach lines. This external pressure field in turn feeds back into the boundary layer and affects its growth rate [54]. The magnitude of the pressure variations produced in the external flow by the viscous layer can be measured by a hypersonic viscous-interaction parameter χ defined as

$$\chi = \frac{M_\infty^3 \sqrt{C_e}}{\sqrt{R_{ex}}}, \tag{44}$$

where $C_e = \mu/\mu_\infty$ and $R_{ex} = \rho_\infty u_\infty x/\mu_\infty$. M_∞ is the free stream Mach number when x approachs infinity. The strong and weak interaction regions are described by Anderson: [55]

Strong interaction $\chi > 3$,
Weak interaction $\chi < 3$.

At our prediction step, pressure distribution along x-direction is given by curve fitted expression,

$$\frac{p}{p_\infty} = \frac{1 + 0.660\chi + 0.158\chi^2}{1 + 0.321\chi}, \tag{45}$$

which is a composite formula fit for both strong interaction region and weak one [56]. This approximation was fit for perfect air flow over adiabatic wall with $\gamma = 1.4$ and $P_r = 1$. In boundary layer approximation, pressure is a function of x alone at certain flow conditions. When pressure distribution along x direction is given by Eq. (45), the development of boundary layer is calculated by solving Eqs. (31) to (34).

A correction step is used to recalculate the distribution of pressure after the shape of boundary layer is given in prediction step. Outside of boundary layer, the external flow is approximated by an isentropic flow across a single family of Mach lines and is governed by the Prandtl-Mayer relation:

$$\frac{\partial P}{\partial \theta} = \frac{\gamma M_e^2}{\sqrt{M_e^2 - 1}}, \tag{46}$$

where

$$\theta = \tan^{-1} \frac{\partial \delta^*}{\partial x}, \tag{47}$$

δ^* is the displacement thickness of boundary layer ,and M_e, the Mach number at the edge of the boundary layer, where the external inviscid flow and viscous boundary layer flow match each other. The corrected pressure distribution is calculated by numerical integration of Eq. (46). The corrected solution of boundary layer is obtained by solving Eqs. (31) to (34) one more time with new pressure distribution. We assume Mach waves emanating from the edge of the boundary layer. Along the Mach line, flow parameters such as pressure, velocity, temperature and density are constant and equal to corresponding values at the edge of boundary layer, which are given by viscous solution. The angle between Mach line and x-direction equal to sum of θ and Mach angle. Because temperature in free stream is low, frozen flow is a good approximation for external flow. The complete final solution is combination of viscous boundary layer solution and inviscid isentropic external solution. Similarly, we can get the solution for perfect gas by boundary layer approach.

Results and Discussion

Hypersonic O_2 flow past a thin flat plate with adiabatic wall is studied as a test case to validate our code. Perfect gas model and thermochemically nonequilibrium gas model are used respectively in order to study the real gas effects. To analysis the stability of hypersonic boundary layer flow, we introduce the disturbance to the mean flow by blowing and suction through a slot on the wall and compare present results with results in linear stability theory (LST). The specific flow conditions are:

$M_\infty = 10$ $\quad T_\infty = 350.0\,K$
$p_\infty = 3903.5Pa$ $\quad Pr = 0.72$
$Re_\infty = \rho_\infty U_\infty/\mu_\infty = 6.6 \times 10^6/m$

The computational domain and grids are shown in Fig. 1, where the grid spacing is conventional wall-clustered and vertical scale has been enlarged by a factor of 3 for clarity.

Mean flow

As a part of validation, steady mean flow is calculated by both DNS and boundary layer approach.

Perfect Gas

Figure 2 shows the pressure contours computed by DNS and boundary layer approximation separatedly. The blank region in the up left corner of the figure shows that the pressure in this region is uniform, which is because that the pressure is given as uniform at the entrance. The figures shown here is far from the entrance in order to reduce the effect of entrance conditions. As shown in the figure, there are a bunch of Mach waves emanating from the edge of the boundary layer. The angle between Mach line and x-direction given in DNS exactly equals to that in boundary layer approach, which is approximated as sum of θ defined in Eq. 47and Mach angle. Because non-reflecting boundary condition is used at upper boundary, there is no numerical Mach waves reflected at the upper boundary. It is obvious that pressure is almost constant across the boundary layer and along the Mach lines. The distribution of pressure along the surface is shown in Fig. 3. As a result of interaction of inviscid external flow and viscous boundary layer flow, there are significant pressure gradients in streamwise direction especially in the upstream. This kind of interaction becomes weaker and weaker with the development of boundary layer. However, the Mach waves propagate to the downstream and strongly change the free stream in the downstream, which is shown in the profiles of vertical velocity and pressure in downstream (Figs. 4 and 5), where $x = 0.0945m$. On the contrary, the profiles of temperature and streamwise velocity in downstream are not strongly affected by Mach waves(Figs. 6 and 7). Except for the little differences in wall temperature, there is good agreement with profiles of velocity, temperature and pressure calculated by DNS and boundary layer approach.

Reacting Gas

Figure 8 shows the comparison of pressure contours computed by DNS and boundary layer approach. Same as perfect gas case, the blank region in the up left corner is due to uniform pressure given at entrance. In external flow, the temperature is low, the performance of frozen flow is same as perfect gas flow. The Mach lines calculated by DNS match that obtained by boundary layer prediction. The distribution of pressure along the surface is shown in Fig. 9. Near the wall, the temperature is very high so that oxygen moleculae begin to dissociate. The contours of dissociated oxygen are shown in Fig. 10. The change of atomic oxygen mass fraction (C_o) along the surface is shown in Fig. 11. With the C_o increasing along the all, wall temperature keeps decreasing(Fig. 12). The difference between translational temperature and vibrational temperature indicates that the vibrational energy is in nonequilibrium on the wall as well as inside of boundary layer(Fig. 13). The velocity, density and mass fraction profiles at the location $x = 0.0945m$ are shown in Figs. 14 to 17. Overall, the profiles of flow variables are in good agreement between DNS and boundary layer prediction. The reacting gas results of temperature are compared with perfect gas results in Figs. 18 and 19. For perfect gas, the wall temperature is much higher than that that of reacting gas. As a result, the thickness of boundary layer for perfect gas is larger than reacting flow, which may change the property of the most amplified second mode disturbance [57].

Unsteady flow

In this section, the generation of instability waves by introducing disturbance to mean flow through localized wall suction and blowing is considered. According to Balakumar and Malik's study [58], such forcing would generate several discrete modes as well as continuous spectra. The particular form of forcing used in present study is

$$v_w(x) = A(x)\sin(\omega t) \tag{48}$$

where $A(x)$ is constructed by using sine-function which is shown in Fig. 20. The instantaneous flow is modeled by a mean flow plus perturbations of flow variables, $\phi = \bar{\phi} + \phi'$ (ϕ stands for $u, v, p, \rho_1, \rho_2, T$ or T_v). It is to be noted that the $A(x)$ is carefully chosen so that the nondimensionalized amplitude of perturbation is at least one-order larger than the maximum numerical noise, and it can not be too large to avoid the distortion of mean flow. The unsteady computations are carried out for more than 30 periods in time till the solutions reach a periodic state. After that, unsteady computations are conducted for one additional period in time. FFT is performed on the results of the unsteady flow in one period to obtain Fourier amplitude and phase angle of perturbations of flow variables throughout the flow field,

$$\phi'(x, y, t) = |\phi'| e^{i[\psi'(x,y) - \omega t]}. \tag{49}$$

For perfect gas flow, present results are also compared with local parallel analyses. The LST code is developed by Hu and Zhong [59]. Thus, the fluctuations are decomposed in a normal mode form

$$\phi'(x,y,t) = \hat{\phi}(y)e^{i(\alpha x - \omega t)} \tag{50}$$

where $\hat{\phi}$ is complex amplitude of the disturbance, $\alpha = \alpha_r + i\alpha_i$, the streamwise wave number. Compared Eq. (50) with (49), streamwise wave number can be extracted in DNS as

$$\alpha_i = -\frac{1}{|\phi'|}\frac{d|\phi'|}{dx} \tag{51}$$

$$\alpha_r = \frac{d|\psi'|}{dx} \tag{52}$$

The response of flow field to the forcing from blowing and suction is analyzed in the following sections.

Perfect Gas

Three different frequencies are chosen to be enforced in blowing and suction. The frequencies nondimensionalized by $\omega_0(\omega_0 = u_\infty/L,\ L = 0.021m)$ are $6\pi, 8\pi, 10\pi$ and 12π respectively.

Mode Structure of Instability Waves

Figure 21 shows the contours of instantaneous pressure perturbation after the flow field reaches a periodic state . In this case, dimensionless frequency equals to 10π (corresponding nondimensional frequencies expressed in term of $F = \frac{\omega\mu_\infty}{\rho_\infty u_\infty^2} = \frac{\omega}{\omega_0 R_{eL}} = 2.267\times10^{-4}$). It is clear that blowing and suction introduce boundary layer disturbance as well as Mach waves radiation. Due to the weak discontinuity property of Mach wave, there is numerical oscillation in the region existing Mach waves, where the high order difference schemes have no enough dissipation. The instantaneous contours of entropy and vorticity perturbation are plotted in Figs. 22 and 23. It is obvious that maximum perturbation of entropy appears near the edge of boundary layer while vorticity perturbation concentrates near the wall region. Because external flow including Mach waves are approximately isentropic where viscosity is neglectable, the radiation of Mach waves has no direct effects on entropy waves and vorticity waves. The pressure perturbation along the surface for four cases of different frequencies is shown in Fig. 24, while corresponding growth rate defined in Eq. (52) is shown in Fig. 25. According to Eq. (50), it is stable if $\alpha_i > 0$, and it is unstable if $\alpha_i < 0$. It is hard to determine if the flow is stable or not here, because the computational domain is still in the range of effect of disturbance sources, blowing and suction.

Comparison with LST Results

The preliminary calculations of linear stability analysis at the location $x = 0.025m$ and $x = 0.030m$ have been carried out. For different frequency, the complex wave numbers of discrete modes are computed by searching eigenvalues in LST. The real component of wave number at fixed enforced frequency is given by Eq. (52) in DNS. The comparison of dimensionless wave number (nondimensionalized by length scale $L = 0.021m$) predicted by DNS and LST is tabulated in Table 1.

Location X (m)	ω/ω_0	$\alpha_r L$ (DNS)	$\alpha_r L$ (LST)
0.025	6π	21.081	19.988
	8π	27.262	26.241
	10π	34.567	33.156
0.030	6π	18.121	19.796
	8π	26.027	26.305
	10π	34.089	33.010

Table 1. Comparison of real components of wave number calculated by DNS and LST ($L = 0.021m$).

The comparison of eigenfunctions calculated by DNS and LST is shown in Figs. 26 to 28 for $\omega/\omega_0 = 10\pi$ case at location $x = 0.025m$. The results agree reasonably well considering the fact that LST is based on a parallel flow assumption. It is clear that the real component of eigenfunctions of pressure perturbation is strongly effected by Mach wave, which can not be captured by LST. The mode structure inside the boundary layer shows that it is the second mode dominant at this location according to Mack's [7] results.

Reacting Gas

For reacting flow, the nondimensionalized frequencies enforced in blowing and suction are $8\pi, 10\pi$ and 12π respectively. Figure 29 shows the contours of instantaneous pressure perturbation after the flow field reaches a periodic state . In this case, dimensionless frequency equals to 10π. The pressure perturbation contours of reacting gas are very similar to that of perfect gas (Fig. 21) , so is true for contours of entropy and vorticity perturbation. The instantaneous contours of vibrational temperature and dissociated oxygen density perturbation are plotted in Figs. 30 and 31. It is obvious that maximum perturbation of vibrational temperature appears near the edge of boundary layer while dissociated

oxygen density perturbation concentrates near the wall region as well as the edge of boundary layer, which are not significantly effected by radiation of Mach waves. For dimensionless frequency of 10π case, the effect of amplitude of disturbance enforced in blowing and suction is studied by increasing $A(x)$ shown in Fig. 20 to 5 times. The amplified disturbance case is denoted as case $A.2$, while the unamplified case is denoted as case $A.1$. After obtaining the perturbation field, the fluctuation amplitude of flow variables in case $A.2$ is adjusted by a factor of 0.2, and plot together with the case $A.1$. Fig. 32 shows the dimensionless perturbation amplitude of pressure and temperature along the wall surface. The distribution of velocity perturbation amplitude along streamwise direction at different locations in wall-normal direction is shown in Fig. 33. The amplitude contours of atomic oxygen mass fraction and pressure perturbation are compared in Figs. 34 and 35. Due to the linearity of enforced disturbance, the perturbation field of case $A.1$ is almost identical to the adjusted perturbation field of case $A.2$, which indicates that the amplitude of disturbance introduced here is appropriate. The eigenfunctions at location $x = 0.025m$ are shown in Figs. 38 to eigvt-r-p. The pressure perturbation along the surface for three cases of different frequencies is shown in Fig. 36, while corresponding growth rate defined in Eq. (52) is shown in Fig. 37. Further study is needed to study the effect of frequencies on stability waves.

Conclusions

This paper has applied and tested a high-order upwind finite difference method for simulation of reacting oxygen flow over a flat plate. Spectral method and computational code for boundary layer approach are developed to provide initial condition for direct numerical simulation as well as validation of mean flow of DNS. There is good agreement for the mean flow between DNS results and locally self-similar results from boundary layer approach. Blowing and suction through the slot on the wall is enforced as the source of disturbance to study the stability of boundary layer. For perfect gas, the eigenvalues and eigenfunctions calculated by DNS and LST agree reasonably well considering the fact that LST is based on a parallel flow assumption. Work is currently underway to parallelize our code for further study of the stability and real gas effects.

Acknowledgements

This research was supported by the Air Force Office of Scientific Research under grant numbers F49620-97-1-0030 and F49620-00-1-0101 monitored by Dr. Len Sakell.

References

[1] Th. Herbert and M. V. Morkovin. Dialogue on Bridging Some Gaps in Stability and Transition Research. *In Laminar-Turbulent Transition, IUTAM Symposium, Stuttgart, Germany, 1979, R. Eppler, H. Fasel, Editors, pp. 47–72*, Springer-Verlag Berlin, 1980.

[2] M. V. Morkovin and E. Reshotko. Dialogue on Progress and Issues in Stability and Transition Research. *In Laminar-Turbulent Transition, IUTAM Symposium, Toulouse, France, 1989, D. Arnal, R. Michel, Editors*, Springer-Verlag Berlin, 1990.

[3] E. Reshotko. Boundary Layer Instability, Transition and Control. *AIAA paper 94-0001*, 1994.

[4] Th. Herbert. Progress in Applied Transition Analysis. *AIAA paper 96-1993*, 27th AIAA Fluid Dynamics Conference, New Orleans, LA, June, 1996.

[5] L. Lees and C. C. Lin. Investigation of the Stability of the Laminar Boundary Layer in Compressible Fluid. *NACA TN No. 1115*, 1946.

[6] L. M. Mack. Boundary Layer Stability Theory . *Rept. 900-277*, Rev. A, Jet Propulsion Lab., Pasadena, CA, 1969.

[7] L. M. Mack. Boundary layer linear stability theory. In *AGARD report, No. 709*, 1984.

[8] L. M. Mack. Stability of Axisymmetric Boundary Layers on Sharp Cones at Hypersonic Mach Numbers. *AIAA Paper 87-1413*, 1987.

[9] M. R. Malik. Transition in Hypersonic Boundary Layers. 1989. Fourthe Symposium on Numerical and Physical Aspects of Aerodynamic FLows, January 16-19, 1989,State University, Long Beach, CA. .

[10] M. R. Malik, R. E. Spall, and C.-L. Chang. Effect of Nose Bluntness on Boundary Layer Stability and Transition. *AIAA paper 90-0112*, 1990.

[11] P. W. Duck. The inviscid axisymmetric stability of the supersonic flow along a circular cylinder. *J. Fluid Mechanics*, 214:611, 1990.

[12] G. Gasperas. The Stability of the Compressible Boundary Layer on a Sharp Cone at Zero Angle of Attack. *AIAA Paper 87-0494*, 1987.

[13] M. Simem and U. Dallmann. On the Instability of Hypersonic FLow past a Pointed Cone- Comparison of Theoritical and Experimental Results at Mach 8. *DLR-FB 92-02*, , 1992.

[14] H. L. Reed, W. S. Saric, and D. Arnal. Linear Stability Theory Applied to Boundary Layers. *Annual Review of Fluid Mechanics*, Vol. 28, pp. 389-428 1996.

[15] M. R. Malik. Stability theory for chemically reacting flows. In D. Arnal and R. Michel, editors, *Laminar-Turbulent Transition, IUTAM Symp., Toulouse, Springer-Verlag*, 1990.

[16] M. R. Malik and E. C. Anderson. Real Gas Effects on Hypersonic Boundary-Layer Stability. *Physics of Fluids A*, Vol. 3, No. 5, pp. 803-19, 1991.

[17] G. S. Stuckert and H. L. Reed. Linear Disturbances in Hypersonic, Chemically Reacting Shock Layers. *AIAA Journal*, Vol. 32, No. 7, pp. 1384-1393, 1994.

[18] M. L. Hudson, N. Chokani, and G. V. Candler. Linear stability of hypersonic flow in thermochemical nonequilibrium. *AIAA Paper 96-0671*, 1996.

[19] E. Reshotko and N.M.S. Khan. Stability of the Laminar Boundary Layer on a Blunt Plate in Supersonic Flow. *IUTAM Symposium on Laminar-Turbulent Transition, R. Eppler and H. Fasel, editors*, Springer-Verlag, Berlin, pp. 186-190, 1980.

[20] J. M. Kendall. Wind Tunnel Experiments Relating to Supersonic and Hypersonic Boundary-Layer Transition. *AIAA Journal*, Vol. 13, No. 3, pp. 290–299, 1975.

[21] A. Demetriades. Laminar Boundary Layer Stability Measurements at Mach 7 Including Wall Temperature Effects. *AFOSR-TR-77-1311*, November, 1977.

[22] K. F. Stetson, E. R. Thompson, J. C. Donaldson, and L. G. Siler. Laminar Boundary Layer Stability Experiments on a Cone at Mach 8, Part 1: Sharp Cone. *AIAA paper 83-1761*, January 1983.

[23] J. L. Potter and J. D. Whitfield. Effects of Slight Nose Bluntness and Roughness on Boundary-Layer Transition in Supersonic Flows. *Journal of Fluid Mechanics*, Vol. 12, part 4, pp. 501–535, 1962.

[24] E. J. Softly, B. C. Graber, and R. C. Zempel. Experimental Observation of Transition of the Hypersonic Boundary Layer. *AIAA Journal*, Vol. 7, No. 2, pp. 257-263 1969.

[25] K. F. Stetson, E. R. Thompson, J. C. Donaldson, and L. G. Siler. Laminar Boundary Layer Stability Experiments on a Cone at Mach 8, Part 2: Blunt Cone. *AIAA paper 84-006*, January 1984.

[26] Th. Herbert and V. Esfahanian. Stability of Hypersonic Flow over a Blunt Body. *AGARD CP-514*, pp. 28-1 – 12, April, 1993.

[27] E. Kufner, U. Dallmann, and J. Stilla. Instability of Hypersonic Flow Past Blunt Cones – Effects of Mean Flow Variations. *AIAA paper 93-2983*, June 1993.

[28] E. Kufner and U. Dallmann. Entropy- and Boundary Layer Instability of Hypersonic Cone Flows – Effects of Mean Flow Variations. *IUTAM Symposium on Laminar-Turbulent Transition*, Sendai/Japan, September 1994, pp. 197-204, Springer-Verlag, Berlin, 1994.

[29] F. P. Bertolotti and Th. Herbert. Analysis of the Linear Stability of Compressible Boundary Layers Using the PSE. *Theoretical and Computational Fluid Dynamics*, Vol. 3, pp. 117–124, 1991.

[30] C.L. Chang, M.R. Malik, G. Erlegacher and M.Y. Hussaini. Compressible Stability of Growing Boundary Layers Using Parabolized Stability Equations. *AIAA paper 91-1636*, 1991.

[31] N.M. El-Hady. Nonparallel Instability of Supersonic and Hypersonic Boundary Layers. *Physics of Fluids*, Vol. 3, No. 9, pp. 2164, 1991.

[32] D. Arnal. Predictions based on linear theory. In *AGARD report, No. 793*, 1994.

[33] C.L. Chang and M.R. Malik. Non-parallel Stability of Compressible Boundary Layers. *AIAA paper 93-2912*, 1993.

[34] J.A. Masad and A.H. Nayfeh. Effect of heat transfer on the stability of compressible boundry layers. *Computers and Fluids*, 21, 1992.

[35] H. Vinh C.-L. Chang and M.R. Malik. Hypersonic boundery-layer stability with chemical reactions using pse. *AIAA paper 97-2012*, 1997.

[36] M. Morkovin. On the Many Faces of Transition. *Viscous Drag Reduction*, C.S. Wells, editor, Plenum, 1969.

[37] E. Reshotko. Environment and receptivity. In *AGARD report, No. 709*, 1984.

[38] E. Reshotko. Hypersonic stability and transition. *in Hypersonic Flows for Reentry Problems, Eds. J.-A. Desideri, R. Glowinski, and J. Periaux, Springer-Verlag*, 1:18–34, 1991.

[39] M. V. Morkovin. Transition at Hypersonic Speeds. *ICASE Interim Report 1*, NASA CR 178315, May, 1987.

[40] L. S. G. Kovasznay. Turbulence in supersonic flow. *Journal of the Aeronautical Sciences*, 20(10):657–682, October 1953.

[41] J. F. Mckenzie and K. O. Westphal. Interaction of linear waves with oblique shock waves. *The Physics of Fluids*, 11(11):2350–2362, November 1968.

[42] M. Nishioka and M. V. Morkovin. Boundary-Layer Receptivity to Unsteady Pressure Gradients: Experiments and Overview. *Journal of Fluid Mechanics*, Vol. 171, pp. 219-261 1986.

[43] M. E. Goldstein and L. S. Hultgren. Boundary-Layer Receptivity to Long-Wave Free-Stream Disturbances. *Annual Review of Fluid Mechanics*, Vol. 21, pp. 137-166 1989.

[44] W. S. Saric, H. L. Reed, and E. J. Kerschen. Leading edge receptivity to sound: Experiments, dns, and theory. *AIAA Paper 94-2222*, 1994.

[45] X. Zhong. Direct Numerical Simulation of Hypersonic Boundary-Layer Transition Over Blunt Leading Edges, Part II: Receptivity to Sound . *AIAA paper 97-0756, 35th AIAA Aerospace Sciences Meeting and Exhibit, January 6-9, Reno, Nevada*, 1997.

[46] Y. Ma and X. Zhong. Numerical simulation of transient hypersonic flow with real gas effects. AIAA Paper 99-0416, AIAA, 1999.

[47] C. Park. *Nonequilibrium Hypersonic Aerothermodynamics*. Wiley Interscience, 1990.

[48] C. Park. Review of chemical-kinetic problems of future nasa missions, i: Earth entries. *Journal of Thermophysics and Heat Transfer*, 7:385–398, 1993.

[49] X. Zhong. High-Order Finite-Difference Schemes for Numerical Simulation of Hypersonic Boundary-Layer Transition. *Journal of Computational Physics*, 144:662–709, 1998.

[50] X. Zhong. Additive Semi-Implicit Runge-Kutta Schemes for Computing High-Speed Nonequilibrium Reactive Flows. *Journal of Computational Physics*, Vol. 128, pp. 19-31, 1996.

[51] T. Gökçen. *The Computation of Hypersonic Low Density Flows with Thermochemical Nonequilibrium*. PhD thesis, Stanford University, 1989.

[52] T. J. Poinsot and S. K. Lele. Boundary conditions for direct simulations of compressible viscous flows. *J. of Computational Physics*, 101:104–129, 1992.

[53] Y. Liu and M. Vinokur. Nonequilibirum flow computations i. an analysis of numerical formulations of conservation laws. *Journal of Computational Physics*, 83:373–397, 1989.

[54] L. Lee and R.F. Probstein. *Hypersonic Viscous Flow over a Flat Plate*. Princeton University, Aeronautical Engineering Laboratory, 1952.

[55] J. D. Anderson Jr. *Hypersonic and High Temperature Gas Dynamics*. McGraw-Hill, Inc., 1989.

[56] M. Rasmussen. *Hypersonic Flow*. John Wiley and Sons, Inc., 1994.

[57] M. L. Hudson, N. Chokani, and G. V. Candler. Nonequilibrium effects on hypersonic boundary layers and inviscid stability. *AIAA Paper 94-0825*, 1994.

[58] P. Balakumar and M.R. Malik. Discrete modes and continuous spectra in supersonic boundary layers. *Journal of Fluid Mechanics*, 239:631–656, 1992.

[59] S. H. Hu and X. Zhong. Linear Stability of Compressible Couette Flow. *AIAA paper 97-0432*, 1997.

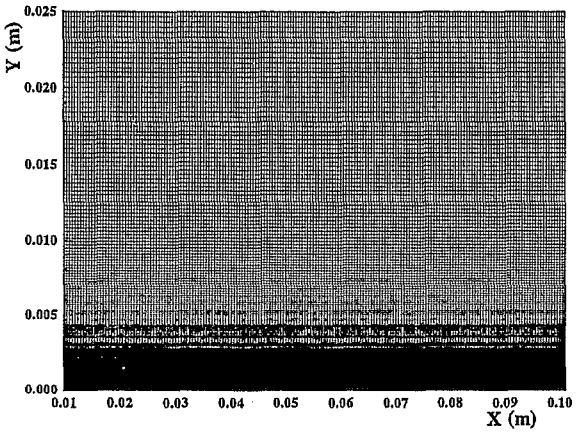

Figure 1: Computational domain and grids for hypersonic flow over a flat plate.

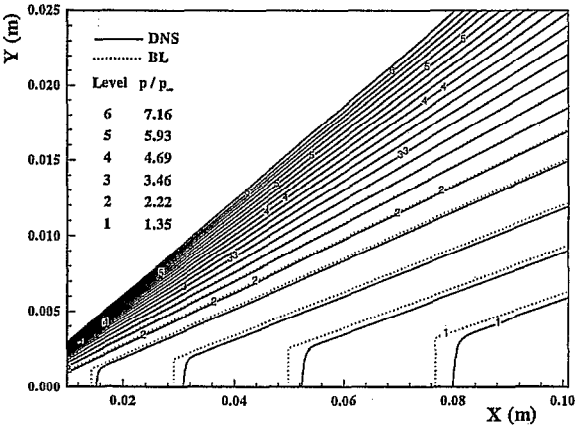

Figure 2: Comparison of pressure contours computed by DNS and boundary layer approximation (perfect gas).

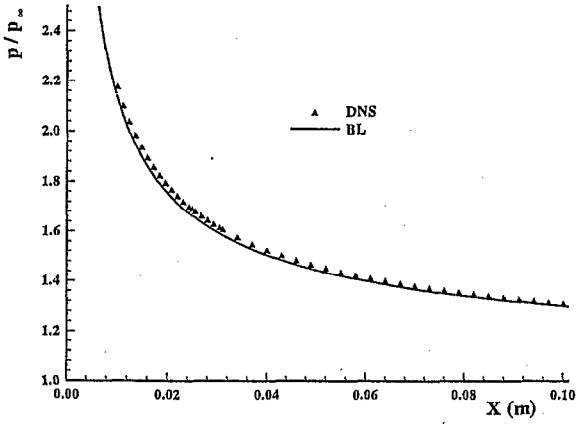

Figure 3: Comparison of pressure distribution on the wall surface computed by DNS and boundary layer approximation (perfect gas).

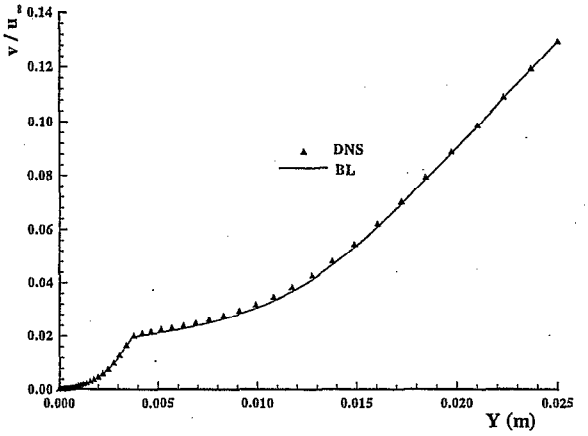

Figure 4: Profiles of vertical velocity at $X = 0.0945m$ (perfect gas).

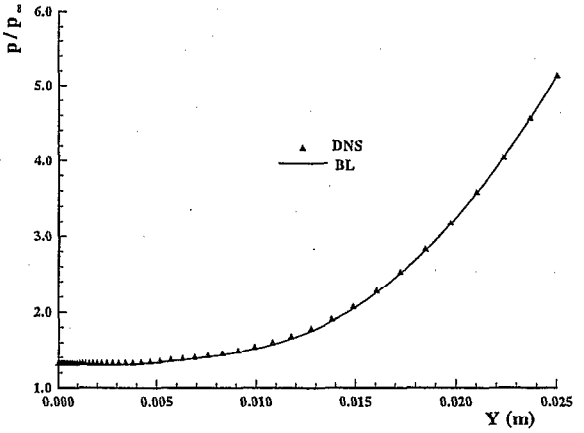

Figure 5: Profiles of pressure at $X = 0.0945m$ (perfect gas).

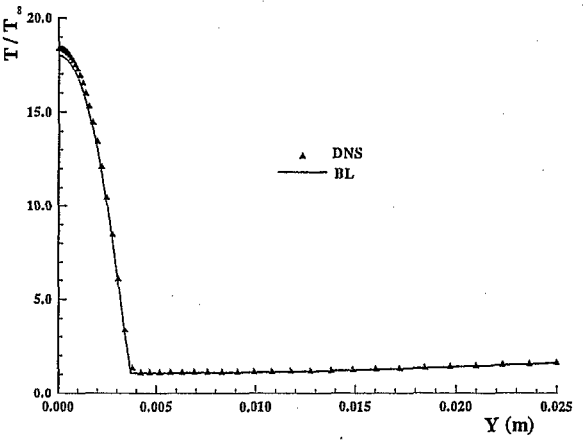

Figure 6: Profiles of mean temperature at $X = 0.0945m$ (perfect gas).

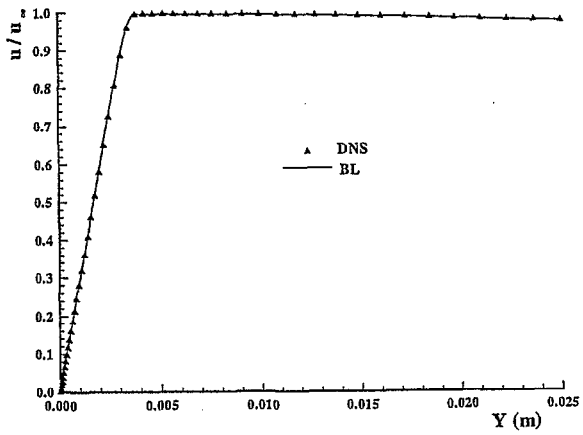

Figure 7: Profiles of streamwise velocity at $X = 0.0945m$ (perfect gas).

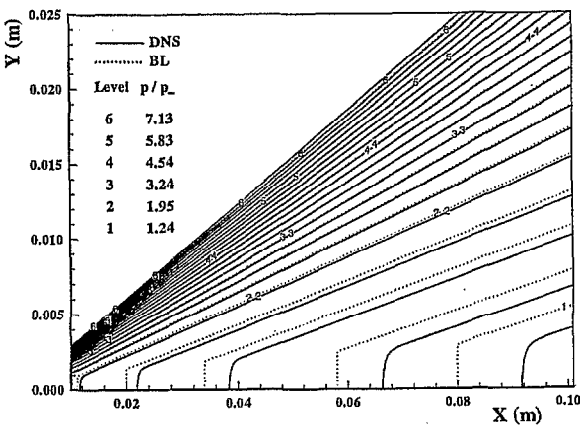

Figure 8: Comparison of pressure contours computed by DNS and boundary layer approximation (reacting gas).

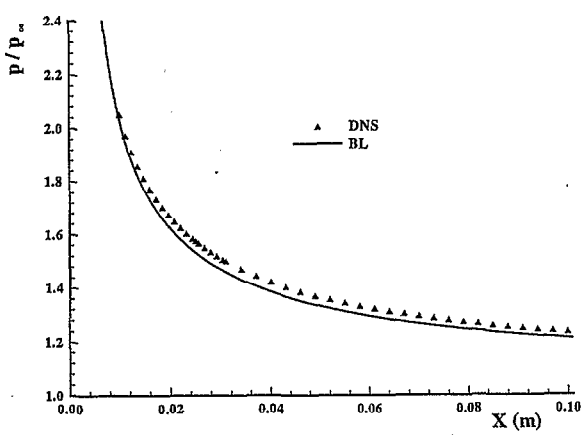

Figure 9: Comparison of pressure distribution on the wall surface computed by DNS and boundary layer approximation (reacting gas).

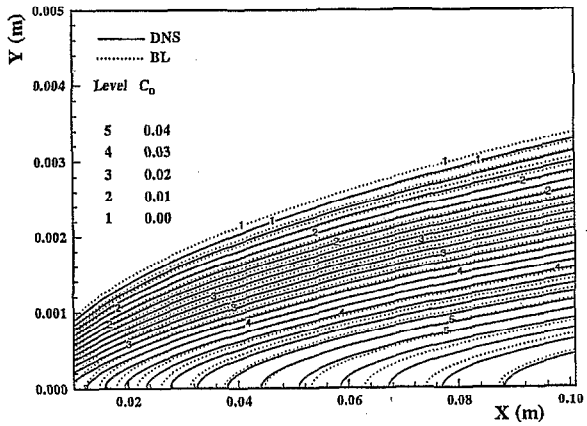

Figure 10: Comparison of contours of dissociated oxygen mass fraction computed by DNS and boundary layer approximation (reacting gas).

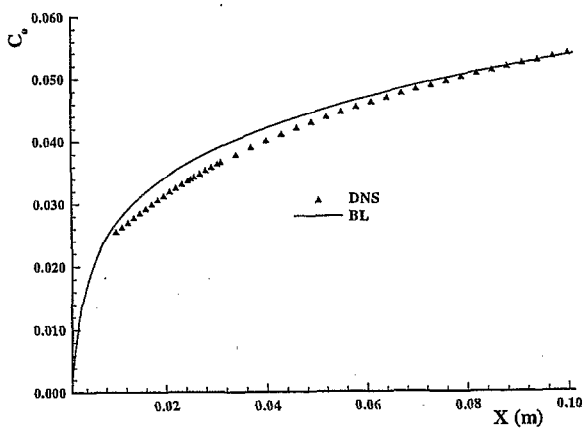

Figure 11: Comparison of dissociated oxygen mass fraction on the wall surface computed by DNS and boundary layer approximation (reacting gas).

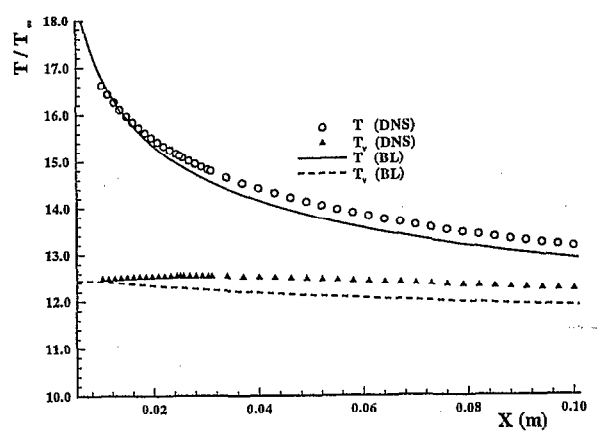

Figure 12: Comparison of temperature distribution on the wall surface computed by DNS and boundary layer approximation (reacting gas).

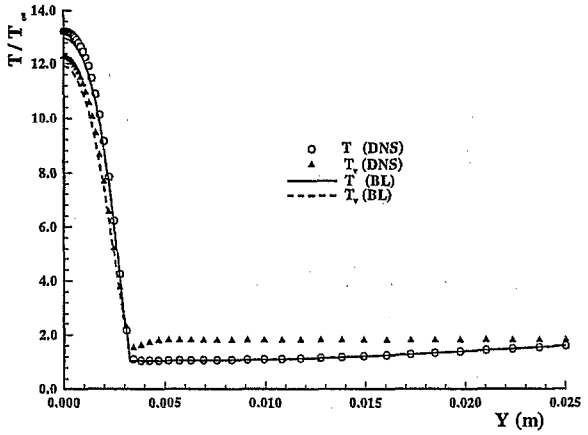

Figure 13: Profiles of temperature at $X = 0.0945m$ (reacting gas).

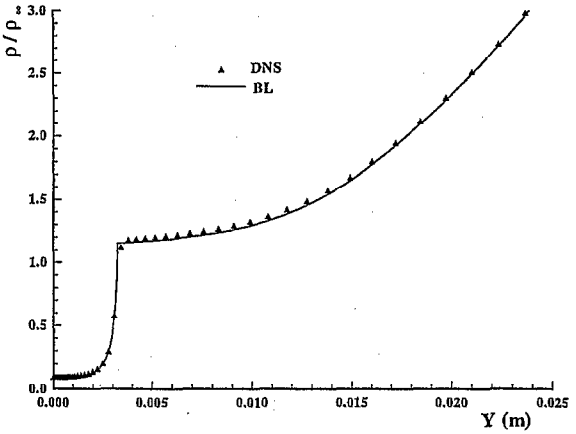

Figure 16: Profiles of mean density at $X = 0.0945m$ (reacting gas).

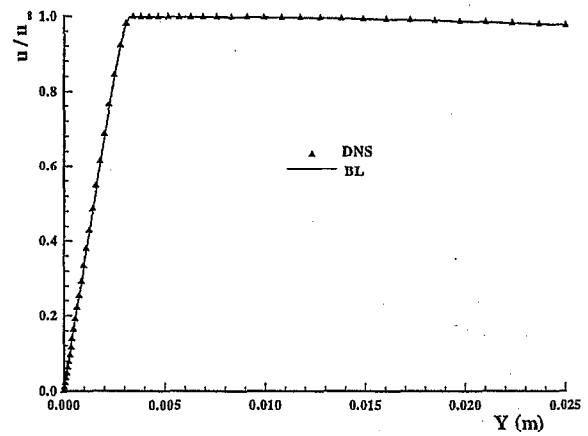

Figure 14: Profiles of streamwise velocity at $X = 0.0945m$ (reacting gas).

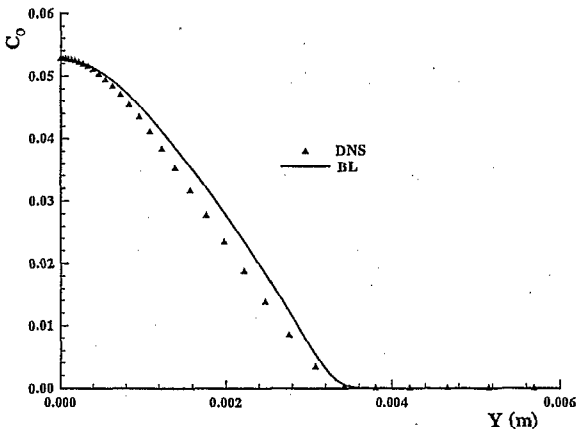

Figure 17: Profiles of dissociated oxygen mass fraction at $X = 0.0945m$ (reacting gas).

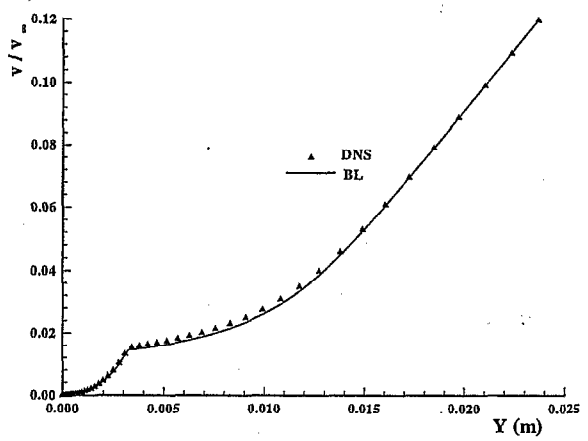

Figure 15: Profiles of vertical velocity at $X = 0.0945m$ (reacting gas).

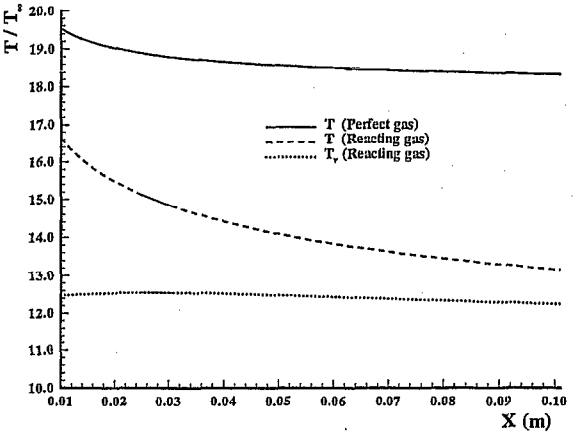

Figure 18: Comparison of mean wall temperature between perfect gas and reacting gas.

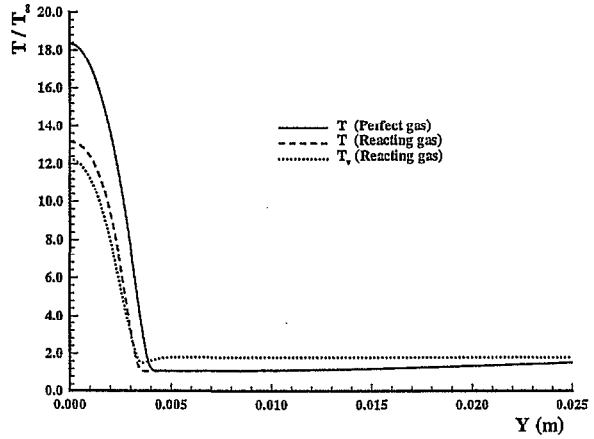

Figure 19: Comparison of mean temperature profiles between perfect gas and reacting gas at $X = 0.0945m$.

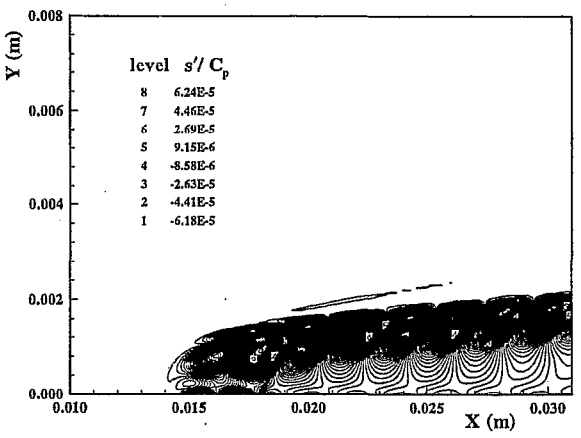

Figure 22: Contours of instantaneous entropy perturbation for the case of $\omega/\omega_0 = 10\pi$ (perfect gas).

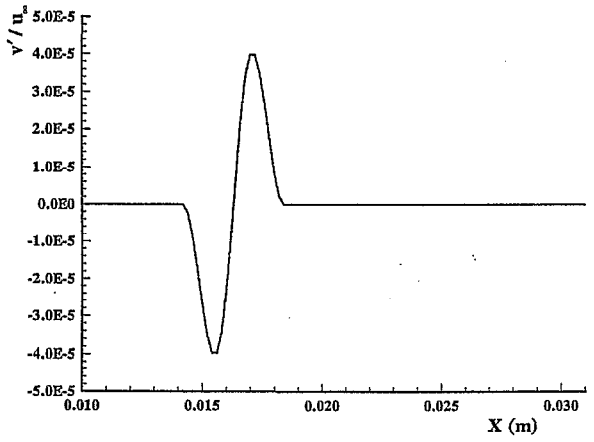

Figure 20: Vertical velocity distribution over blowing and suction slot for generating disturbances.

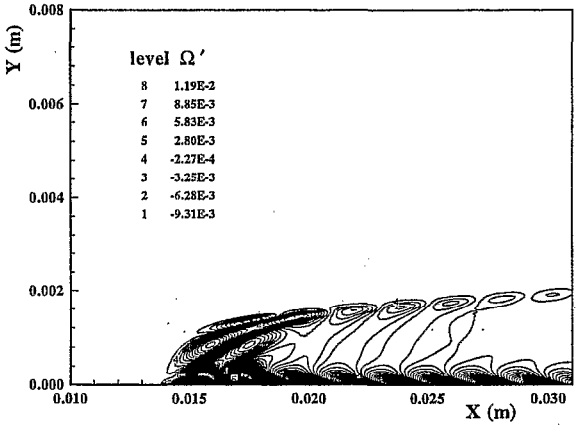

Figure 23: Contours of instantaneous vorticity perturbation for the case of $\omega/\omega_0 = 10\pi$ (perfect gas).

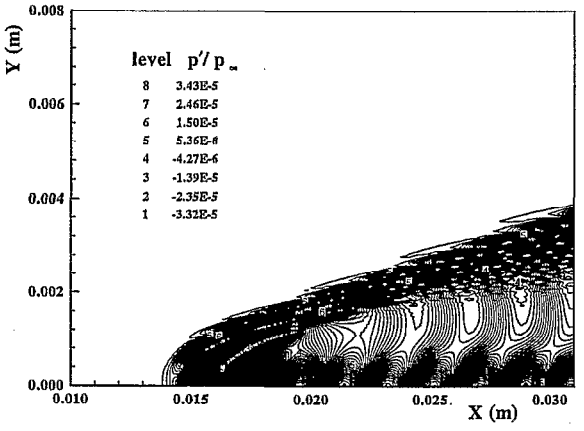

Figure 21: Contours of instantaneous pressure perturbation for the case of $\omega/\omega_0 = 10\pi$ (perfect gas).

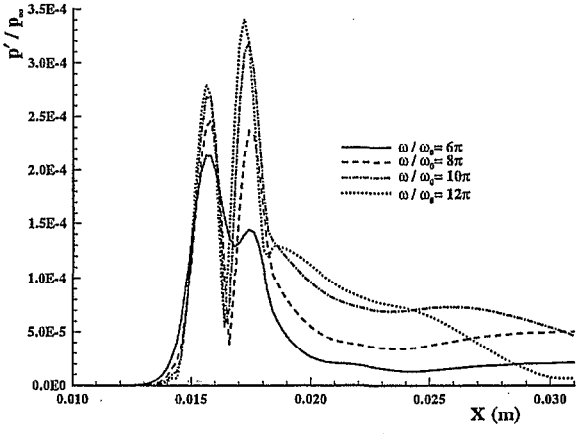

Figure 24: Distribution of the peak amplitudes of the pressure perturbation along the wall surface for four cases of different frequencies.

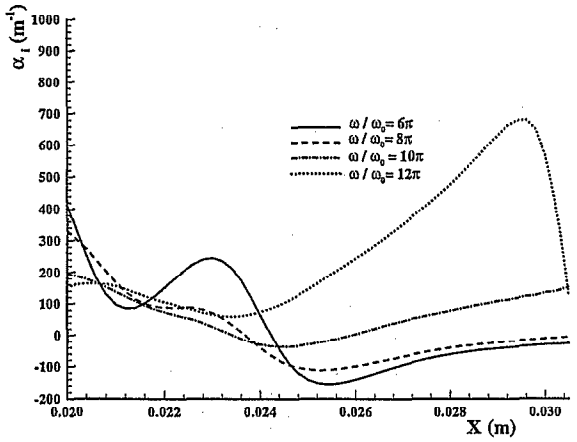

Figure 25: Distribution of the local growth rate along the wall surface for four cases of different frequencies.

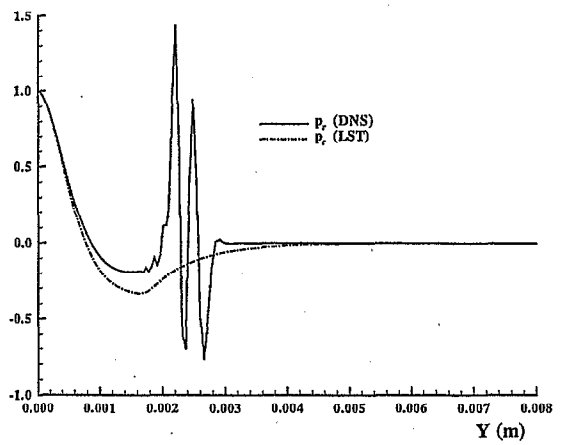

Figure 28: Comparison of disturbance eigenfunction of pressure for the case of $\omega/\omega_0 = 10\pi$ at $X = 0.025m$ (perfect gas).

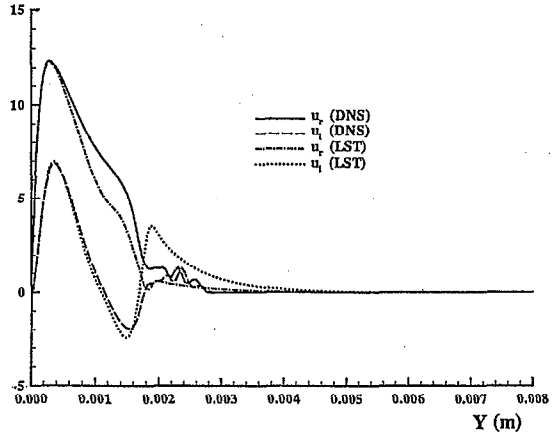

Figure 26: Comparison of disturbance eigenfunction of streamwise velocity for the case of $\omega/\omega_0 = 10\pi$ at $X = 0.025m$ (perfect gas).

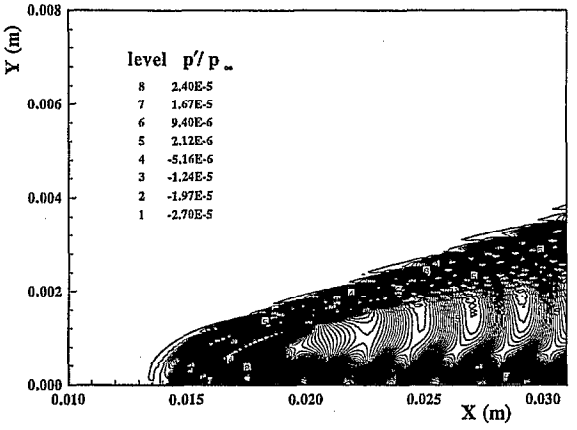

Figure 29: Contours of instantaneous pressure perturbation for the case of $\omega/\omega_0 = 10\pi$ (reacting gas).

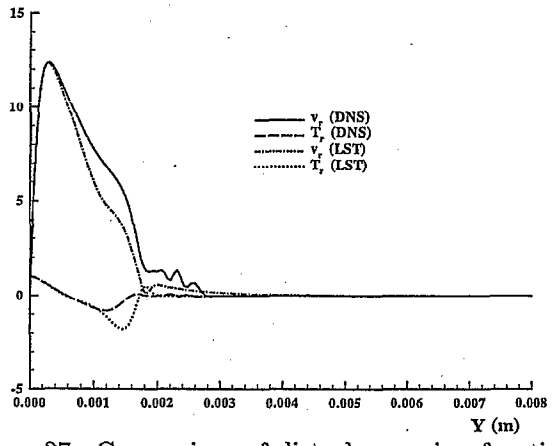

Figure 27: Comparison of disturbance eigenfunctions of temperature and vertical velocity for the case of $\omega/\omega_0 = 10\pi$ at $X = 0.025m$ (perfect gas).

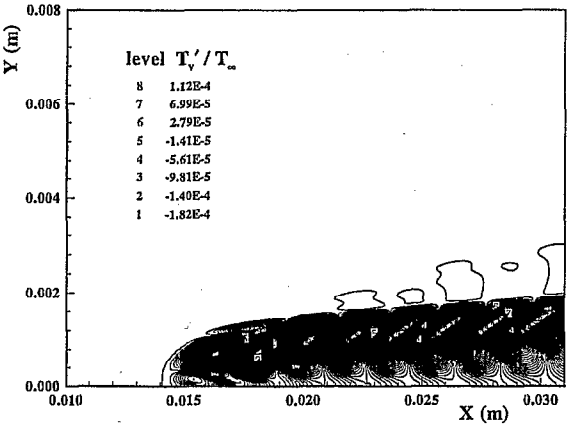

Figure 30: Contours of instantaneous vibrational temperature perturbation for the case of $\omega/\omega_0 = 10\pi$ (reacting gas).

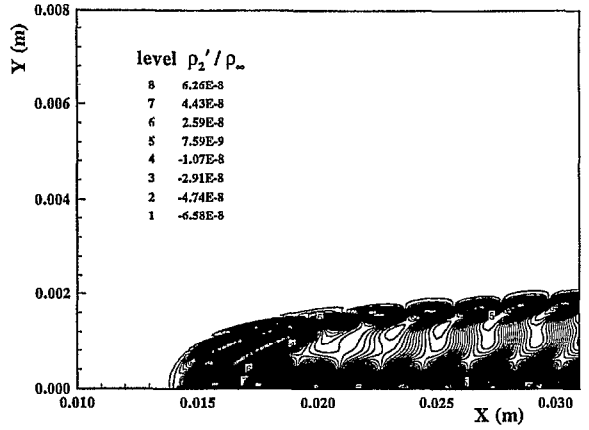

Figure 31: Contours of instantaneous dissociated oxygen density perturbation for the case of $\omega/\omega_0 = 10\pi$ (reacting gas).

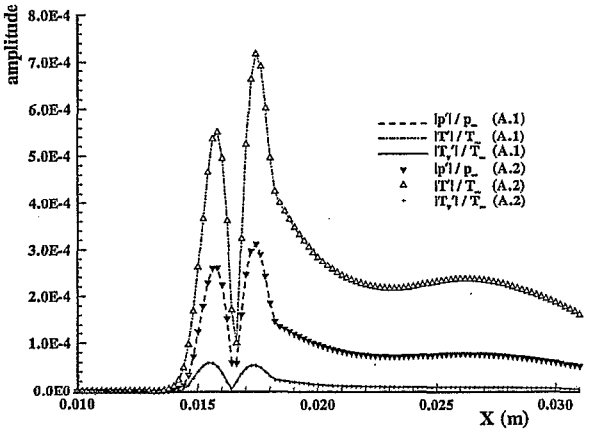

Figure 32: Comparison of perturbation amplitude of pressure and temperature along the wall surface for the case of $\omega/\omega_0 = 10\pi$ (reacting gas).

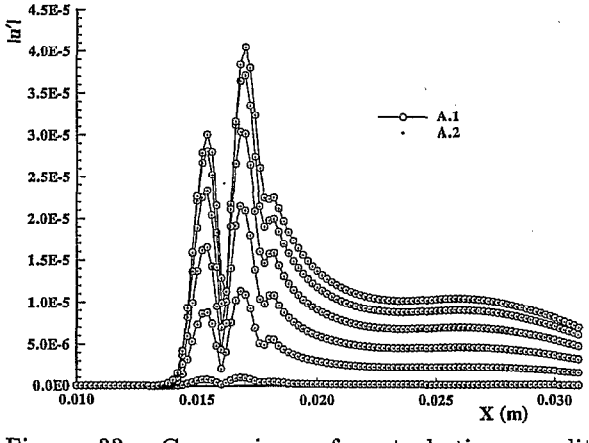

Figure 33: Comparison of perturbation amplitude of streamwise velocity at different locations($j = 2, 12, 22, 32, 42, 52$) for the case of $\omega/\omega_0 = 10\pi$ (reacting gas).

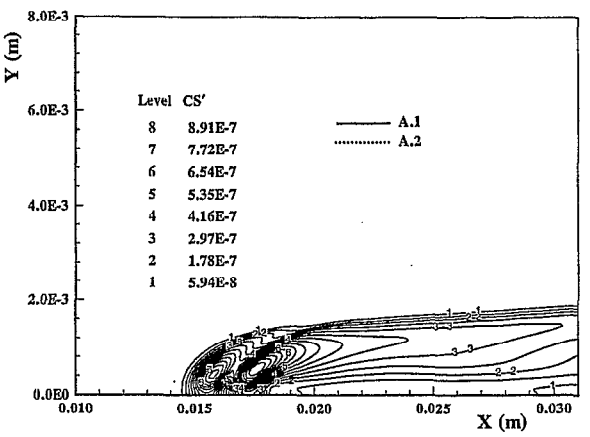

Figure 34: Comparison perturbation amplitude contours of dissociated oxygen mass fraction for the case of $\omega/\omega_0 = 10\pi$ (reacting gas).

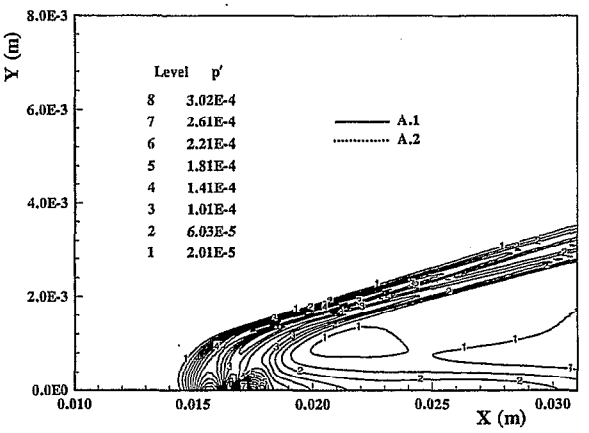

Figure 35: Comparison perturbation amplitude contours of pressure for the case of $\omega/\omega_0 = 10\pi$ (reacting gas).

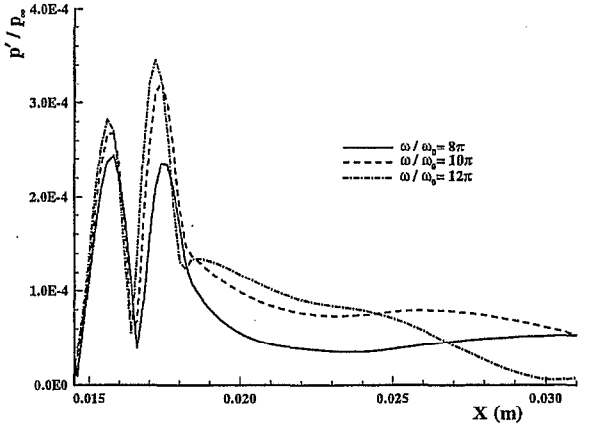

Figure 36: Distribution of the peak amplitudes of the pressure perturbation along the wall surface for three cases of different frequencies (reacting gas).

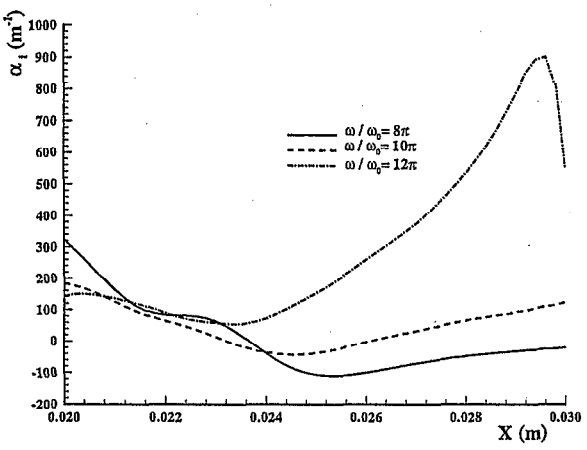

Figure 37: Distribution of the local growth rate along the wall surface for three cases of different frequencies (reacting gas).

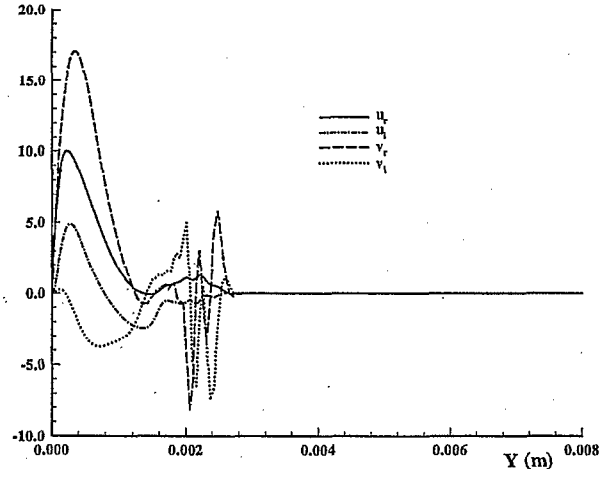

Figure 38: Disturbance eigenfunctions of velocity for the case of $\omega/\omega_0 = 12\pi$ at $X = 0.025m$ (reacting gas).

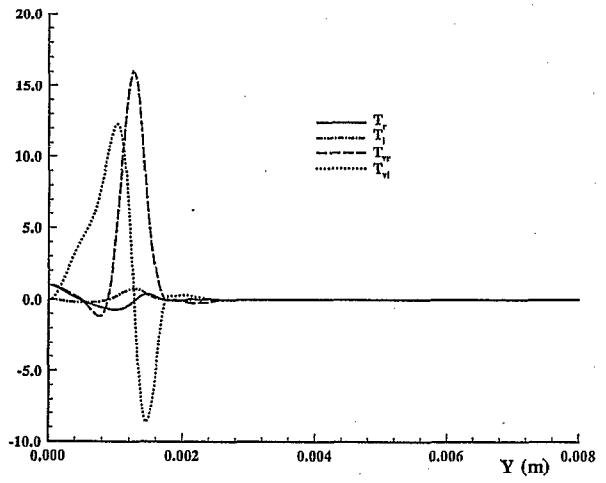

Figure 39: Disturbance eigenfunctions of temperature for the case of $\omega/\omega_0 = 12\pi$ at $X = 0.025m$ (reacting gas).

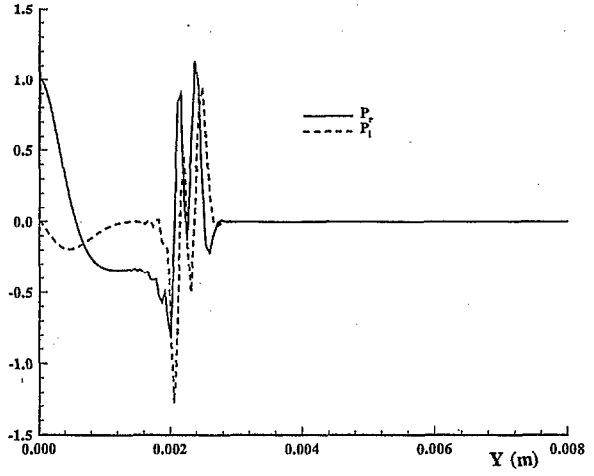

Figure 40: Disturbance eigenfunctions of pressure for the case of $\omega/\omega_0 = 12\pi$ at $X = 0.025m$ (reacting gas).